Research Square

Preprints are preliminary reports that have not undergone peer review. They should not be considered conclusive, used to inform clinical practice, or referenced by the media as validated information.

AI-enabled, implantable, multichannel wireless telemetry for photodynamic therapy

Woo Seok Kim
Texas A&M University https://orcid.org/0000-0002-3075-1847
M. Ibrahim Khot
University of Leeds https://orcid.org/0000-0002-5062-2284
Hyun-Myung Woo
Texas A&M University
Dong-Hyun Baek
Sun Moon University
Sungcheol Hong
Texas A&M University
Thomas Maisey
University of Leeds https://orcid.org/0000-0003-1555-7699
Brandon Daniels
Texas A&M University
Patricia Coletta
University of Leeds
Byung-Jun Yoon
Texas A&M University https://orcid.org/0000-0001-9328-1101
David Jayne
University of Leeds https://orcid.org/0000-0002-8725-3283
Sung Il Park (sipark@tamu.edu)
Texas A&M University https://orcid.org/0000-0003-0001-8967

Article

Keywords: photodynamic therapy, photosensitizer, colorectal cancer, artificial intelligence, wireless optoelectronic devices, wireless power transmission, Monte Carlo simulation

Posted Date: March 18th, 2021

DOI: https://doi.org/10.21203/rs.3.rs-315921/v1

License: This work is licensed under a Creative Commons Attribution 4.0 International License.
Read Full License

Abstract

Photodynamic therapy (PDT) is an alternative method for treating cancers, and its outcomes are highly dependent on light delivery to tumor cells to activate a photosensitizer. Existing approaches paired with advances in wireless technologies enable remote delivery of light to tumors but suffer from poor spatiotemporal resolution due to inabilities to minimize oxygen depletion in a tumor. Here, we introduce AI-informed low-power wireless telemetry with an integrated thermal/light simulation platform that bypasses all constraints above. The simulator leads to the optimized combination of wavelengths and light sources, and AI-assisted wireless telemetry uses the parameters from the simulator to enable adequate illumination of tumors through high-throughput (< 20 mice) and multi-wavelength operation. They establish a range of guidelines for effective PDT regimen design. Hypericin and Foscan mediated PDT demonstrated substantial suppression of tumor growth, suggesting that the proposed platform provides the potential for widespread use in fundamental research and/or clinical settings.

Introduction

Photodynamic therapy (PDT) is an anti-cancer treatment modality, which has the advantage of targeting cancer cells, while minimizing toxicity in normal healthy tissue[1,2]. PDT involves the administration of a photosensitizer which is taken up and retained within tumors. Activation of the photosensitizer is mediated by light of a specific wavelength. In the clinical setting, this is conventionally achieved through the use of high-powered lasers. In the presence of oxygen, the excited photosensitizer can lead to the production of reactive oxygen species, inducing intracellular oxidative stress and triggering tumor cytotoxicity. Oxygen, a photosensitizer, and light are key factors for PDT, and their importance is supported by *in vivo* and *in vitro* studies that provide insights into the mechanisms of action[3–5]. For example, tissue oxygenation in tumors is critical for the production of oxygen free radicals and successful phototoxicity. Tumor hypoxia is a limiting factor to the efficacy of PDT[6,7]. Similarly, the delivery and selective uptake of photosensitizers into tumors are vital for optimal PDT efficacy, while reducing adverse toxicities[8,9]. Finally, light delivery and the use of fractionated light to minimize oxygen depletion in tumors are important when designing effective photodynamic regimens[10]. However, the effort to optimize PDT outcomes through the manipulation of the three factors has probably reached a plateau either due to an insufficient understanding of the mechanism by which a concentration ratio between cancer and normal cells occurs or due to poor spatiotemporal resolution at which current techniques deliver light and/or a photosensitizer to cancer cells.

Recent advances in wireless technologies have enabled wireless control of light delivery to tumor cells in a freely behaving animal with improved spatiotemporal resolutions[11–13]. Biocompatible miniaturized optoelectronic devices utilize electromagnetic (EM) wave propagation at a high frequency (HF) or ultra-high frequency (UHF) range to convert radio frequency (RF) energy into optical energy using a single wavelength of light sources[14–16]. Although these approaches have some utilities, the activation of a photosensitizer by a single wavelength of light sources is limited. For example, Foscan has two peaks at

406 nm and 652 nm with different absorption rates, respectively[17]. This indicates that 78 % of light absorbance at 406 nm can contribute to the generation of oxygen-free radicals that selectively kill tumor cells. One way to compensate for loss is to increase light intensity, however, its efficacy is marginal. Furthermore, increases in light intensity correspond to increased heat generation, which damages normal tissues[18–20]. Another complication involves tissue damage associated with absorptions of UHF range EM waves into biological tissues[21–23]. EM waves at UHF ranges (300 MHz ~ 3 GHz) are not transparent to EM waves, and exposure to UHF EM waves would lead to tissue heating and therefore damage surrounding tissues. These prevent the widespread use of wireless approaches in PDT studies.

Here, we introduce a new class of the integrated platform that bypasses all constraints described above. It combines an artificial intelligence (AI)-informed low-power wireless telemetry system with a Monte Carlo (MC) thermal/light simulation. The integrated thermal/light MC simulation platform via a user-friendly software interface yields a PDT regimen (e.g., choice of wavelengths, determination of the number of light sources, and its placement onto an implantable device) to be most effective in hindering tumor growth. The AI-assisted low-power wireless telemetry system uses the parameters from the platform to enable the most effective PDT. The utilization of an advanced AI algorithm for automated video analysis allows for real-time tracking of the freely moving animals in a cage to ensure robust activation of animals (implantable devices) in cages. Optimized delivery of PDT via a miniaturized multichannel optoelectronic device implanted in the animals permits selective controls over multi-wavelength light sources to deliver adequate and uniform light delivery to tumors. Together with an advanced time-division multiplexing strategy using a single RF power source, the proposed wireless system allows for activations of multiple animals (< 5 mice) in multiple home cages up to 4. Under such high-throughput settings, one can facilitate efforts to perform fundamental research within reasonable timelines.

Results

An overview of the proposed integrated platform appears in Fig. 1a. The platform includes 1) integrated MC thermal/light simulation software for optimized PDT regimens, 2) an AI-enabled real-time motion tracking algorithm for animals in a cage, and 3) a low-power wireless telemetry system for activation of a photosensitizer in a high-throughput manner. Integrated MC simulation platform leads to an optimum configuration of light color and source location for effective PDT such as via a user-friendly software interface. Depending on the size of tumors and type of photosensitizer, one can determine light colors (wavelengths), the number of light sources, and their formation onto an implanted device (Fig.1b). This results in the most effective PDT regimen. AI-enabled wireless telemetry uses the parameters from MC simulation to implement PDT. Here, an advanced AI algorithm allows for real-time motion tracking of multiple mice (<5) in a home cage through automated video analysis. This enables the optimal control of prearranged coil-antennas to offer uniform wireless coverage and thereby the robust activation of implantable devices (Fig. 1c). Time-division multiplexing strategy paired with the AI permits simultaneous/independent controls of multiple devices or animals (< 20) in multiple cages (< 4) (Fig. 1d).

In Fig. 1d, two images demonstrate activations of multiple devices in 4 cages (bottom to the left) and mode of switching operation between two different configurations of light sources (bottom to the middle), respectively. Video 1 and 2 provide visual evidence of device operation.

MC simulations for light delivery and heat management

Fig. 2a shows an overview of the integrated MC simulation platform. The platform enables numerical analysis (Monte Carlo theory) of 1) the propagation and absorption of light (photon) and 2) heat dissipation in tissue (skin) and tumor via a user-friendly software interface (Fig. 2a and Supplementary Fig. 1). With the selection of the photosensitizer type, the number of light sources, light colors, and its formation, the integrated simulator performs the analysis. It yields the results for heat dissipation, light absorption, and delivery of light energy to tumors. This allows one to determine a PDT regimen to be most effective in suppressing tumor growth. Figs. 2b-d display representative results for each photosensitizer; Hypericin and Foscan, each of which has peaks at 590 & 542 nm, and 406 & 652 nm, respectively. Here, we utilize a three-dimensional model (8 cm^3) where a sphere object (representing a tumor cell; 4 mm in diameter) is embedded and light sources are placed on top of a tumor model. We also use light sources with 590 nm wavelength for Hypericin and a combination of 406 and 652 nm for Foscan. Fig. 2b shows heat maps and plots of heat dissipation as a function of wavelength by constant (right to the top) and duty cycled illumination (right to the bottom). Results revealed that no detectable change in temperatures at given parameters, ensuring no damage to surrounding tissues by thermal dissipation from light sources during device operation with 25 % duty-cycle lighting. It is supported by measurement results (Supplementary Fig. 2). Figs. 2c and d summarize performance comparisons in five criteria (degree of light penetration, rate of energy absorbance, level of uniformity of energy absorbance into a tumor cell, the time required for delivery of targeted light energy, and range of temperature variation) and show distributions of light absorption into a tumor cell for Hypericin and Foscan, respectively. Results performed under different conditions (wavelength) revealed that uniform light delivery and minimum heat dissipation for Hypericin are reached with light sources (wavelength of 590 nm) and 25 % of duty-cycle operation while those for Foscan are optimized at a condition (light sources with a combination of 406 and 652 nm and 25 % duty cycle operation). These are validated *in vivo* and *in vitro* experiments. Detailed information on simulation results is found in Supplementary Figs. 3 and 4.

AI-enabled real-time motion tracking of multiple animals

Fig. 3a illustrates step-by-step procedures for AI-enabled real-time motion tracking of mice in a cage where five mice with a device implanted freely behave and four coil antennas are installed. Here, we use two pairs of X-shaped coil antennas, each of which is responsible for the optimal power delivery according to the motion of an animal along the x-axis or y-axis (Fig. 3a-(1)). A webcam on the top of the cage sends a stream of images to the custom-trained DeepLabCut (DLC)[24] model at the rate of 25 fps (Fig. 3a-(1)). As a frame arrives, the trained DLC model detects the locations of the snouts and tails, each of which has a confidence score for the prediction (Fig. 3a-(2)). The decision threshold for what the AI

model appraises as detection is set to 0.6, and any predicted body part with a confidence score below 0.6 is discarded. Next, the AI model quantifies the matching score between all possible combinations of the detected body parts (Fig. 3a-(3)). Based on the matching scores, the AI model finds the optimal one-to-one mapping between the detected snouts and tails via the maximum weighted bipartite matching (Fig. 3a-(4))[25]. Once the model completes the assignment of each snout-tail pair to every mouse, one can determine the orientation of each mouse in a cage (Supplementary Fig. 5). This leads to the identification of the optimal coil antenna index for th mouse (Fig. 3a-(5)), and creates a control signal for antenna selection. Supplementary Fig. 6 shows a representative example of an image processed by the algorithm. Once the controller receives the signal from the AI result, it activates one of the coil antennas. This results in optimum wireless power delivery to mice (implanted devices) (Fig. 3a-(6)). The procedures from (1)-(6) are repeated.

For assessment of the proposed AI algorithm, we use a metric, defined as the percentage of correct predictions for the data tested[26]. Fig. 3b shows antenna selection accuracy for three different antenna settings: 1) two pairs of X-shaped antenna coils, one pair of X-shaped coil aligning with 2) the x- or 3) y-axis. Results revealed that the AI algorithm guarantees the accuracy of 80 % or above in every setting that we tested (Fig. 3b). Figs. 3c and d show statistics of the number of frames for two representative cases; how long a selected antenna remains activated (Fig. 3c) and how many frames (or long interval times) it takes between activation of an antenna and reactivation of itself after the first deactivation (Fig. 3d). It is likely that some occupants, not all of them, in a cage may not receive enough power for activation of a photosensitizer due to a decision by the AI (e.g., when two mice or vectors along the length of their body are aligned with the x-axis and corresponding vectors for the rest three mice are on the y-axis, the AI chooses an antenna coil that offers better wireless coverage in the y-direction). Experimental results revealed that discharges of power stored in an embedded supercapacitor can last longer than the time intervals shown in Supplementary Figs. 7 and 8. This suggests that the proposed AI-based algorithm paired with the use of a supercapacitor ensures robust activation of devices in a cage. Detailed information on evaluations of the AI algorithm is found in Method section.

Low-power multichannel wireless telemetry

Fig. 4a highlights signal flow from the TX controller to antenna coils installed in each cage. Low-power wireless telemetry system employs a time-division multiplexing strategy to allow for the use of a single power source. When combined with a supercapacitor embedded in an implanted device, the proposed system enables simultaneous control of multiple cages up to 4. Measurement results show that an implantable device maintains constant light intensity during off cycles and thereby ensures robust activation of a photosensitizer (Fig. 4b). Most important to the multi-wavelength operation is a novel actuation mechanism by which an individual channel is selected. Fig. 4c illustrates a switching mechanism by a reed switch. When the TX system transmits a long pulse signal with an interval of few seconds to an implantable device, a reed switch embedded in an implantable device responds to it and triggers an output of circuitry involved (Fig. 4d and Video 1). This results in reversible switching between two channels. Fig. 4e shows images of a device with two different modes of switching operation. Ch1

activates 4 inner light sources in violet while Ch2 selects 4 peripheral light sources in red. Note that a reed switch enabled switching mechanism requires only tens of A which is a few hundred fold reductions in power consumption compared with microcontroller employed actuation mechanisms[16,27–30]. The detailed layout and components information of the dual-channel device are in Supplementary Fig. 9, and the working principle is described in Supplementary Fig. 10.

Hypericin and Foscan mediated *in vivo* / *in vitro* PDT

To highlight the potential therapeutic application of the proposed AI-enabled wireless telemetry system, PDT was evaluated *in vivo* and *in vitro* in pre-clinical models of colorectal cancer. Initially, the LED surface operating temperatures were monitored over 2 days during continuous LED operation. No significant change in temperature was found over 48 hours (Hour 0 vs. Hour 48; 0.3°C increase, p=0.15) (Fig. 5a). Next, Hypericin (photosensitizer) mediated PDT was performed in HT29 colorectal cells, utilizing the LED devices to photoactive Hypericin.

A 70 % reduction in cell viability was observed between Hypericin-treated cells kept in the dark and treated cells irradiated with light (p=0.003) (Fig. 5b). Following this, the PDT mediating activity of the wireless LED devices was evaluated *in vivo* in murine models of colorectal cancer. As shown in Fig. 5c, devices were surgically implanted subcutaneously onto the right dorsal flanks of mice and positioned adjacent to HT29 tumor xenografts. Over 7 days of continuous PDT treatment, HYP(+)LED(+) treated mice demonstrated the largest effect in suppressing tumor growth (Fig. 5d). By Day 7, HYP(+)LED(-) treated mice and HYP(-)LED(+) treated mice groups exhibited 29-fold increase (p<0.01) and 9-fold increase (p<0.05) in tumor volumes, as compared to the HYP(+)LED(+) group. In addition, negligible changes in mice weights were recorded over the PDT treatment period in all treatment groups (Day 0 vs. Day 7: HYP(+)LED(+) p=0.52, HYP(+)LED(-) p=0.37 and HYP(-)LED(+) p=0.1) (Fig. 5e). Histological analysis of HT29 tumor xenografts confirms PDT mediated cytotoxicity in the HYP(+)LED(+) treated group, which was not observed in the HYP(+)LED(-) and HYP(-)LED(+) groups (Fig. 5f). Histological analysis also confirmed no systemic toxicity of treatment in mice livers (Supplementary Fig. 11). To illustrate the advantage of combined dual-wavelength PDT over single wavelength PDT, Foscan treated HT29 cells were subjected to red LEDs light treatment or combined red/violet LEDs light treatment. Using red LEDs only, a 58 % cell viability was observed, as compared to 14 % cell viability in combined red/violet LEDs treated cells (Fig. 5g).

Discussion

Most photosensitizers have more than one peak in their light absorption spectrum, and photoactivation of the photosensitizers using two or more different wavelengths can enhance the efficacy of PDT. A light source such as blue (450 nm), yellow (590 nm), and red (650 nm) LEDs has a different turn-on voltage[31]. When two different wavelengths of light sources are connected in parallel or share a node in a circuit, a voltage at the node becomes regulated by a LED with a lower turn-on voltage (longer wavelength of light sources) and will not reach the necessary threshold for a LED with a higher turn-on voltage (shorter

wavelength of light sources). This results in activation of a single color (longer wavelength of light sources) or imbalanced light illumination. For this reason, implementation of dual- or multi-channel (or colors) in a single platform device requires an actuation mechanism for simultaneous/ independent control of channels. We discussed a variety of scenarios using dual colors light sources using MC simulations to extract parameters that yield the most effective treatment. An actuation mechanism triggered by a reed switch enabled efficient activation of a photosensitizer with power budgets as low as tens of A.

DLC uses deep neural networks for accurate pose estimation of user-defined animal body parts. In this work, we developed a software based on a custom-trained DLC for real-time detection of the snouts and tails of multiple mice in a video frame, where maximum weighted bipartite matching was used to match the snout and tail of each mouse. We used a matched pair of body parts (i.e., snout-tail pair) to infer the orientation of a given mouse, which can subsequently be used to optimally control the TX coil antenna for efficient wireless power delivery. While the proposed algorithm yields fairly accurate predictions as discussed before, we expect that its performance may be further enhanced by incorporating a predictive model that can forecast the orientation of a given animal in the near future. Temporal sequence prediction models, such as recurrent neural networks (RNNs)[32,33], may be used for this purpose, which is currently under investigation. The potential applications also involve quantitative analysis of complex animal behaviors such as their social interactions.

The proposed AI-based algorithm paired with advanced coil antennas enables robust activation of implantable optoelectronic devices in cages. When a normal vector of an implanted device is aligned with that of the TX coil antenna, maximum wireless transmission occurs between two coils[34–36]. When misaligned, the efficiency would significantly drop. In general, reconfiguration of antennas such as adjustment of the gap between a coil and the ground without rematching of impedance is not recommended once they are installed in a cage[37]. By doing that, transmission efficiency can significantly drop. In contrast, animals freely behave in a cage, suggesting that angles or orientations between an implanted device and the TX coil antenna vary at different times. This could be problematic. For example, two vectors become misaligned when an animal leans against a wall of a cage by standing on hind legs or curls up. This results in a significant drop in harvesting efficiency and thereby no activation of a photosensitizer. When combined with an advanced antenna technology and an impedance matching circuit for switching, the proposed AI-based algorithm allows for a selection from prearranged pairs of antennas or adjustment of antenna formation, thereby leads to a realignment of a TX coil antenna with implantable devices, and therefore enables full wireless coverage in a cage.

Simultaneous activation of multiple animals in 4 home cages using a single RF power source is achieved primarily due to a channel isolation strategy and the use of a supercapacitor. Recently, we introduced a novel channel isolation strategy for high-throughput operation[38]. Although it permits independent activation of cages up to 8, it is unable to simultaneously activate cages. A supercapacitor is crucial for the simultaneous activation of multiple cages. When a cage is activated by the TX system, a supercapacitor embedded in an implantable device in the cage can store power. When deactivated, the

supercapacitor can discharge power to light sources until the cage is reselected (Fig. 4b and Supplementary Figs. 7-8). Together, the proposed wireless platform system can promote progress in fundamental research.

Construction of devices and equipment at a low cost and easy access to this technology could accelerate the adoption of the technology in the broader scientific community and promote fundamental research exploring the mechanism of action and clinical application of PDT. The proposed optoelectronic devices consist of inexpensive commercially available components and can be built with 10 hours of effort in standard cleanroom facilities. Dual-coil transmission antennas made of commercially available cheap Cu wires or tapes can be fabricated with 1 hour of effort in standard laboratory facilities, and they are compatible with commercially available HF range power sources. Moreover, the wireless optoelectronic device can accommodate 8 light sources in a single platform at dimensions of 1 cm by 1cm, and a wavelength of light sources is tunable. This suggests that the proposed AI-enabled wireless telemetry could significantly increase the efficacy of the treatment by optimum configurations of light sources and wavelengths tailored to each photosensitizer.

Although this study focused on PDT for colorectal cancer, the proposed technology is equally applicable across the spectrum of solid cancers. PDT has many advantages over conventional chemo/radiotherapy, including reduced systemic toxicity, preservation of normal tissue architecture, and avoidance of drug resistance. However, the true potential of PDT in cancer treatment has yet to be realized. One of the major limitations has been the requirement to deliver light into anatomically hard-to-reach places with sustained light dosing for a cytotoxic effect. The proposed solution, involving a miniaturized, biocompatible, low-power optoelectronic device to deliver light of multiple wavelengths, has the potential to open up the clinical applications of PDT. Obvious clinical applications include adjuvant therapy to treat minimal residual disease following surgical resection and the long-term palliation of cancer recurrence.

Methods

Integrated simulator for heat dissipation and light propagation

We combined two separate MC-based simulations (heat dissipation[39] and propagation/absorption of light[40] (photons) in tissue (skin) and tumor) and created an integrated simulation platform. Here, we used C language-based MFC library to provide a user-friendly software interface. We conducted all simulations on a computer (Intel Core i7-7th gen, 8 GB RAM). The user-application guide of the developed simulation is found in Supplementary Fig. 1.

Modification to DLC model

We utilized, custom-trained, and modified the DLC Python package (Ver. 2.2b7). Specifically, we used the custom-trained DLC model to estimate the locations of the body parts such as snouts and tails of the mice within an image (i.e., video frame). Note that the original DLC python package does not support a real-time processing feature, instead it only runs on video files. Hence, we directly modified the Python

package in such a way that it can infer the locations of the body parts of the mice and estimate the optimal coil antenna through the functional modules, illustrated in Fig. 3a, in a real-time manner. We conducted all experiments including training the DLC on a GPU workstation (Lambda workstation with Intel Core i9-9960X, 128 GB RAM, and two GEFORCE RTX 2080 Ti graphics cards).

Quantitative performance assessment of the AI-enabled motion tracking algorithm

The proposed AI algorithm yields the following information for each frame: 1) the position of the snout and tail of each mouse, 2) the direction in which each mouse is heading toward, and 3) the angle between a vector along the length of each mouse and the y-axis. Based on this information, the algorithm selects an antenna coil that leads to the best wireless coverage in a cage. The following are three antenna settings considered in this study: 1) Two pairs of X-shaped coil antenna, X-shaped coil antenna in 2) the x-axis direction and 3) the y-axis direction. For the quantitative performance assessment of the algorithm, we used three video recordings, each of which is 10 minutes running time. We randomly extracted and evaluated 20 frames from a total of 15,000 frames in each video recording, and repeated the procedures twenty times. For each set of 20 frames, we compared the decision made by the proposed algorithm for each frame in the given set with the one made by a human expert in each antenna setup. Supplementary Fig. 6 shows a representative example of an image (video frame) processed by the algorithm. To check the performance of each antenna setup and implanted devices, we focused on the following two statistics (in terms of the number of frames): how long a selected antenna remains activated (Fig. 3c) and how many frames (i.e., how long of a time interval) it takes between activation of an antenna and its reactivation after the first deactivation (Fig. 3d). Here, a human expert extracted and analyzed the data, which had been processed by the proposed algorithm, in every 20 frames. For Fig. 3c, we chose a mouse (implanted device) from the group and measured how long a selected antenna remains activated or aligned with a vector determined by the mouse as a function of frames. Similarly, for Fig. 3d, we measured a time interval as a function of the number of frames between deactivation of an antenna and subsequent reactivation of it. These were averaged for 20 trials, leading to the statistics shown in Figs. 3b-d.

Device fabrication

The pattern fabrication process began to mount a flexible copper/polyimide (Cu/PI) bilayer film (thickness; 12 μm/18 μm, AC181200RY, DupontTM Pyralux®) onto a glass slide (dimensions, 5.08 cm by 7.62 cm). In the cleanroom facility, we deposited the photoresistor onto the Cu layer for 2 μm thick (AZ 1518, AZ®, recipe; spin-coated at 4,000 r.p.m. for 20 sec), and illuminated UV lights to lithograph patterns for pads and interconnections (EVG610, EV Group, recipe; UV intensity for 100 mJ cm^{-2}). To engrave the photoresistor layer, the Cu/PI film was immersed in developer solution (AZ Developer 1:1, AZ®) for 30 sec and washed with distilled water for 10 sec. Next, immersion in copper etchant (LOT: Z03E099, Alfa AesarTM) for 10 min and rinses with solvents: acetone, methanol, and isopropanol in order, and distilled water for 1 min defined Cu patterns such as interconnections and pads on the flexible PI layer. In the standard laboratory facility, chip components including SMD (surface-mount-device) LEDs, passive

components, and IC components were mounted onto the pattern using a soldering machine. For encapsulations, we applied Polydimethylsiloxane (PDMS) (SylgardTM 184 silicone elastomer kit, Dow®; 10:1 mix ratio) with a dip-coating process (500 μm thick) to the sample, and then it was cured in the oven at 80 ºC for 1 h. These procedures yield a proposed multi-wavelength optoelectronic implant.

Antenna-coil fabrication and wireless, power-control system

We worked with 8-ga bare Cu wire for the sub-antenna coil and Cu tapes (0.635 mm thick by 2.54 cm wide) for the source-antenna coil. The sub-coils were placed under a cage and around all sides of the cage while the source-coil was situated in the center of the crossed-long side of the cage vertically. Impedance matching using Network Analyzer (ENA Series E5063A, Keysight) with a discrete capacitor component yielded source and sub-coils, each of which resonates at 13.56 MHz (the source coil) and 15 MHz (the sub-coils), respectively. Wireless power control systems consisted of a RF power generator (ID ISC.LRM2500-A, FEIG Electronics), and an auto-tunable matching board (ID ISC.DAT-A, FEIG Electronics). For the multi-cage system, it requires a TX controller including an RF multiplexer (ID ISC.ANT.MUX.M8, FEIG Electronics), a control board (nRF52832 Development Kit, Nordic semiconductor), and a customized decoupling multiplexer.

Finite element-methods analysis

For numerical electromagnetic simulations of the proposed antennas structure, we used a finite element-methods analysis tool (Ansys Electromagnetics Suite 17-HFSS, Ansys®) to compute distributions of the electromagnetic field in a home cage. Antenna coils made of copper stripes or wires were modeled to materials with finite conductivity, 58 MS s^{-1}. We figured out the residual dependency of transmitted power on angles and orientations between an implanted device and the TX coil antenna in the experimental box. All simulations were conducted with a TX level of 4 W, which is far below guidelines suggested by IEEE or ICNIRP[41,42] (Supplementary Fig. 12).

Optical and thermal characteristics of the implant device

The residue light intensity, which keeps in response to the capacitance after the cutoff of the power source, was measured using a photodiode and oscilloscope. This was conducted repeatedly in three colored LEDs that have different turn-on voltages. For thermal assessments of wireless devices, we measured heat dissipation of the light sources in a device using an infrared camera (VarioCAM HDx head 600, InfraTech) in two different conditions: a device installed under a sealed bag of saline solution (10 % PBS) instead of a mouse, and a device itself in the cage. The power supply was a function of time at duty cycles of 25 % with a 10 ms pulse train, which is the same as experimental conditions by the wireless TX system.

Materials for PDT in colorectal cancer models

The human colorectal adenocarcinoma cell line, HT29, was obtained from the European Collection of Authenticated Cell Cultures (Salisbury, UK) and cultured in Roswell Park Memorial Institute (RPMI) 1640 Medium plus GlutaMAX™ (Gibco® by Life Technologies™, Paisley, UK) supplemented with 10 % (v/v) Foetal Bovine Serum (FBS) (Sigma-Aldrich, Gillingham, UK). Hypericin and Foscan were obtained from Sigma Aldrich and biolitec Pharma Ltd. (Jena, Germany) respectively and stock solutions of the photosensitizers were prepared in ethanol. Thiazolyl Blue Tetrazolium Bromide (MTT) was obtained from Sigma Aldrich.

Monitoring implantable device operating temperatures

Implantable LED devices were switched on at room temperature and allowed to continuously run for 48 hours. The surface operating temperature of the miniature LEDs was measured over 48 hours using an RS PRO medical infrared thermometer (RS Components Ltd., Corby, UK).

In vitro PDT cytotoxicity

HT29 cells were seeded into 24-well tissue culture plates (Corning Inc., New York, USA) at 2 x 10^5 cells per well and incubated at 37 °C/5 % CO_2/95 % for 24 hours. Cells were then treated with 200 nM Hypericin or 100 nM Foscan in the dark for 16 hours. Cell cultures were then washed with Dulbecco's Phosphate-Buffered Saline (DPBS, Gibco® by Life Technologies™) and Phenol red-free RPMI 1640 medium with L-glutamine (Gibco® by Life Technologies™) supplemented with 10 % (v/v) FBS was added to cultures. LED devices were positioned and affixed in the centre and underneath the wells and switched on. For single-channel LED devices, light treatment lasted for 1 hour at 10 μW cm^{-2}, equating to 36 mJ cm^{-2} of total light dose. For dual-channel LED devices, light treatment lasted for 1 hour at 0.5 μW cm^{-2}, equating to 1.8 mJ cm^{-2} of total light dose. Depending on the experimental conditions, cultures were either irradiated with light or kept in the dark at room temperature. After 24 hours, the MTT cell viability assay was performed by dissolving Thiazolyl Blue Tetrazolium Bromide into Phenol red-free RPMI 1640 medium (MTT solution). Cell media was discarded from cultures and replaced with the MTT solution and cultures were incubated in the dark for 3 hours. The MTT solution was then discarded and formazan crystals were dissolved using propan-1-ol. Optical absorbance values were measured using a Mithras LB 940 Microplate Reader (Ex: 570 nm) (Berthold Technologies Ltd., Harpenden, UK).

In vivo metronomic PDT

The *in vivo* experiment was conducted in accordance with the Animals (Scientific Procedures) Act 1986. Female BALB/c nude mice (6-8 weeks old) were purchased from Charles River UK, Ltd (Margate, UK). One million (1 x 10^6) HT29 cells were suspended in 100μL of FBS-free RPMI and injected subcutaneously into the right dorsal flank area of mice. Inoculated HT29 cells were grown for 8 days to generate heterotopic HT29 colorectal cancer tumor xenografts. Following the growth of tumor xenografts, the miniature implantable LED devices were sterilized in 70 % ethanol, and surgically implanted into mice and the LED-containing probes were positioned adjacent to tumor xenografts. 3M™ Vetbond™ Tissue Adhesive

surgical glue (3M™ United Kingdom PLC., Bracknell, UK) was used to close up the incisions, through where the devices were inserted (Supplementary Fig. 13).

Immediately following the device implantation (Day 0), mice were intraperitoneally injected with 0.5 mg kg^{-1} Hypericin prepared as working solutions in DPBS, and LEDs were switched on. 0.5 mg kg^{-1} Hypericin injections were administered daily. Tumor xenograft volumes and the weights of mice were measured and recorded on Days 0, 2, 4, 6, and 7. HYP(-)LED(+) group received miniature LED light treatment only. HYP(+)LED(-) group received Hypericin treatment only. HYP(+)LED(+) group received both light and Hypericin treatments. Over 7 days, mice received total doses of 3.5 mg kg^{-1} Hypericin (0.5 mg kg^{-1} Hypericin per day) and 12.1J cm^{-2} of light (light fluency rate = 20 μW cm^{-2}). Following the completion of *in vivo* experiment, the mice were euthanized in accordance with Schedule 1 of the Animals (Scientific Procedures) Act 1986 and the tumor xenografts and mice livers were harvested.

Histological Analysis of Tissue

Harvested tumor xenografts and livers were fixed in 4 % (w/v) paraformaldehyde (PFA) for 24 hours and stored in 70 % (v/v) ethanol at 4 °C. Fixed tissue was then embedded into paraffin, sectioned onto glass slides, and subjected to Haematoxylin and Eosin (H&E) staining. Stained slides were imaged using the Nikon Eclipse E1000 Microscope (Nikon UK Ltd, Kingston upon Thames, UK).

Statistical Analysis

Unpaired two-tailed student's *t*-test was used to perform statistical analysis using GraphPad Prism 9 (GraphPad Software, Inc., California, USA). $p<0.05$ was considered to be statistically significant. Data are presented as the mean ± standard deviation.

Declarations

Data availability

The main data supporting the results in this study are available within the paper and its Supplementary Information.

Code availability

The code will be made available upon the submission of a reasonable request to the corresponding authors.

Competing interests

The authors declare no competing interests.

Author contributions

W. Kim designed a dual-channel device and multi-cage transmission system, fabricated devices and antennas, developed and integrated the MC simulation, tested devices and antenna, and generated figures. M. I. Khot conducted the *in vitro* and *in vivo* experiments, analyzed results, and generated figures, H. Woo developed the AI algorithm, and generated figures. D. Baek designed the device prototype. S. Hong conducted circuit and electromagnetic field simulation, developed the heat dissipation simulation, fabricated devices and antennas, tested devices. T. Maisey conducted the *in vitro* and *in vivo* experiments and histological analyses. B. Daniels verified the AI software performance. P. Coletta oversaw the animal experiments. D. G. Jayne provided resources and edited the manuscript. B. Yoon oversaw the development of the AI algorithm and its performance analysis and edited the manuscript. S. Park provided resources and edited the manuscript. W. Kim, M. I. Khot, H. Woo, and S. Park wrote the manuscript. S. Park oversaw all experiments and data analysis.

Acknowledgments

This work was supported by grants from the interdisciplinary X-Grants Program, part of the President's Excellence Fund at Texas A&M University (S. Park, B. Yoon), 2018 NARSARD Young Investigator Awards (S. Park) from Brain & Behavior Research Foundation and National Science Foundation Engineering Research Center for Precise Advanced Technologies and Health Systems for Underserved Populations PATHS-UP (EEC-1648451; S. Park). This work was also supported by a Wellcome Trust Institutional Strategic Support Fund Fellowship (204825/Z/16/Z; M. I. Khot), a National Institute for Health Research (NIHR) Research Professorship (D. G. Jayne), an NIHR Senior Investigator Award (D. G. Jayne) and the NIHR infrastructure at Leeds. The views expressed are those of the authors and not necessarily those of the National Health Service, the NIHR, or the Department of Health. We would like to thank Syed Khawar Abbas (University of Leeds) for performing the surgical implanting procedures. S. Park would like to express thanks to Dr. Coté (Texas A&M University) for general advice.

References

1. Dougherty, T. J. *et al.* Photodynamic Therapy. *JNCI J. Natl. Cancer Inst.* **90**, 889–905 (1998).
2. Dolmans, D. E. J. G. J., Fukumura, D. & Jain, R. K. Photodynamic therapy for cancer. *Nat. Rev. Cancer* **3**, 380–387 (2003).
3. Oleinick, N. L., Morris, R. L. & Belichenko, I. The role of apoptosis in response to photodynamic therapy: What, where, why, and how. *Photochem. Photobiol. Sci.* **1**, 1–21 (2002).
4. Agostinis, P., Buytaert, E., Breyssens, H. & Hendrickx, N. Regulatory pathways in photodynamic therapy induced apoptosis. *Photochem. Photobiol. Sci.* **3**, 721–729 (2004).
5. Dougherty, T. J. An Update on Photodynamic Therapy Applications. *J. Clin. Laser Med. Surg.* **20**, 3–7 (2002).
6. Henderson, B. W. & Fingar, V. H. Relationship of tumor hypoxia and response to photodynamic treatment in an experimental mouse tumor. *Cancer Res.* **47**, 3110–4 (1987).

7. Kizaka-Kondoh, S., Inoue, M., Harada, H. & Hiraoka, M. Tumor hypoxia: A target for selective cancer therapy. *Cancer Sci.* **94**, 1021–1028 (2003).
8. Reddi, E. Role of delivery vehicles for photosensitizers in the photodynamic therapy of tumours. *J. Photochem. Photobiol. B Biol.* **37**, 189–195 (1997).
9. Konan, Y. N., Gurny, R. & Allémann, E. State of the art in the delivery of photosensitizers for photodynamic therapy. *J. Photochem. Photobiol. B Biol.* **66**, 89–106 (2002).
10. Yoon, I., Li, J. Z. & Shim, Y. K. Advance in Photosensitizers and Light Delivery for Photodynamic Therapy. *Clin. Endosc.* **46**, 7 (2013).
11. Bansal, A., Yang, F., Xi, T., Zhang, Y. & Ho, J. S. In vivo wireless photonic photodynamic therapy. *Proc. Natl. Acad. Sci. U. S. A.* **115**, 1469–1474 (2018).
12. Kim, A. *et al.* An Implantable Ultrasonically-Powered Micro-Light-Source (μLight) for Photodynamic Therapy. *Sci. Rep.* **9**, 1–9 (2019).
13. Yamagishi, K. *et al.* Tissue-adhesive wirelessly powered optoelectronic device for metronomic photodynamic cancer therapy. *Nat. Biomed. Eng.* **3**, 27–36 (2019).
14. Park, S. *et al.* Soft, stretchable, fully implantable miniaturized optoelectronic systems for wireless optogenetics. *Nat. Biotechnol.* **33**, 1280–1286 (2015).
15. Shin, G. *et al.* Flexible Near-Field Wireless Optoelectronics as Subdermal Implants for Broad Applications in Optogenetics. *Neuron* **93**, 509-521.e3 (2017).
16. Kim, W. S., Jeong, M., Hong, S., Lim, B. & Park, S. Fully implantable low-power high frequency range optoelectronic devices for dual-channel modulation in the brain. *Sensors (Switzerland)* **20**, 1–14 (2020).
17. Cramers, P. *et al.* Foscan® uptake and tissue distribution in relation to photodynamic efficacy. *Br. J. Cancer* **88**, 283–290 (2003).
18. Welch, A. J. The Thermal Response of Laser Irradiated Tissue. *IEEE J. Quantum Electron.* **20**, 1471–1481 (1984).
19. Jacques, S. L. & Prahl, S. A. Modeling optical and thermal distributions in tissue during laser irradiation. *Lasers Surg. Med.* **6**, 494–503 (1987).
20. Motamedi, M., Rastegar, S., LeCarpentier, G. & Welch, A. J. Light and temperature distribution in laser irradiated tissue: the influence of anisotropic scattering and refractive index. *Appl. Opt.* **28**, 2230 (1989).
21. Guy, A. W. Analyses of Electromagnetic Fields Induced in Biological Tissues by Thermographic Studies on Equivalent Phantom Models. *IEEE Trans. Microw. Theory Tech.* **19**, 205–214 (1971).
22. Johnson, C. C. & Guy, A. W. Nonionizing electromagnetic wave effects in biological materials and systems. *Proc. IEEE* **60**, 692–718 (1972).
23. Phillips, J. L., Singh, N. P. & Lai, H. Electromagnetic fields and DNA damage. *Pathophysiology* **16**, 79–88 (2009).

24. Mathis, A. *et al.* DeepLabCut: markerless pose estimation of user-defined body parts with deep learning. *Nat. Neurosci.* **21**, 1281–1289 (2018).
25. Zhang, Z. *et al.* Pairwise Matching through Max-Weight Bipartite Belief Propagation. in *2016 IEEE Conference on Computer Vision and Pattern Recognition (CVPR)* vols 2016-Decem 1202–1210 (IEEE, 2016).
26. Congalton, R. G. A review of assessing the accuracy of classifications of remotely sensed data. *Remote Sens. Environ.* **37**, 35–46 (1991).
27. Zhang, Y. *et al.* Battery-free, fully implantable optofluidic cuff system for wireless optogenetic and pharmacological neuromodulation of peripheral nerves. *Sci. Adv.* **5**, 1–12 (2019).
28. Mayer, P. *et al.* Flexible and lightweight devices for wireless multi-color optogenetic experiments controllable via commercial cell phones. *Front. Neurosci.* **13**, 1–14 (2019).
29. Mickle, A. D. *et al.* A wireless closed-loop system for optogenetic peripheral neuromodulation. *Nature* **565**, 361–365 (2019).
30. Kim, W. S. *et al.* A soft, biocompatible magnetic field enabled wireless surgical lighting patty for neurosurgery. *Appl. Sci.* **10**, (2020).
31. Maier-Flaig, F. *et al.* Multicolor silicon light-emitting diodes (SiLEDs). *Nano Lett.* **13**, 475–480 (2013).
32. Martinez, J., Black, M. J. & Romero, J. On Human Motion Prediction Using Recurrent Neural Networks. in *2017 IEEE Conference on Computer Vision and Pattern Recognition (CVPR)* 4674–4683 (IEEE, 2017). doi:10.1109/CVPR.2017.497.
33. Kim, B. *et al.* Probabilistic vehicle trajectory prediction over occupancy grid map via recurrent neural network. in *2017 IEEE 20th International Conference on Intelligent Transportation Systems (ITSC)* 399–404 (IEEE, 2017). doi:10.1109/ITSC.2017.8317943.
34. Flynn, B. W. & Fotopoulou, K. Rectifying loose coils. *IEEE Microw. Mag.* 48–54 (2013).
35. Jonah, O., Georgakopoulos, S. V. & Tentzeris, M. M. Orientation insensitive power transfer by magnetic resonance for mobile devices. *2013 IEEE Wirel. Power Transf. WPT 2013* 5–8 (2013) doi:10.1109/WPT.2013.6556868.
36. Liu, D., Hu, H. & Georgakopoulos, S. V. Misalignment sensitivity of strongly coupled wireless power transfer systems. *IEEE Trans. Power Electron.* **32**, 5509–5519 (2017).
37. RamRakhyani, A. K., Mirabbasi, S. & Chiao, M. Design and optimization of resonance-based efficient wireless power delivery systems for biomedical implants. *IEEE Trans. Biomed. Circuits Syst.* **5**, 48–63 (2011).
38. Kim, W. S. *et al.* Organ-specific, multimodal, wireless optoelectronics for high-throughput phenotyping of peripheral neural pathways. *Nat. Commun.* **12**, 157 (2021).
39. Stujenske, J. M., Spellman, T. & Gordon, J. A. Modeling the Spatiotemporal Dynamics of Light and Heat Propagation for InVivo Optogenetics. *Cell Rep.* **12**, 525–534 (2015).
40. Jacques, S. L. Monte Carlo Modeling of Light Transport in Tissue (Steady State and Time of Flight). in *Optical-Thermal Response of Laser-Irradiated Tissue* (eds. Welch, A. J. & van Gemert, M. J. C.)

109–144 (Springer Netherlands, 2010). doi:10.1007/978-90-481-8831-4_5.

41. Varaldo, P. *Exposure to high frequency electromagnetic fields, biological effects and health consequences (100 kHz-300 GHz)*. (2009).
42. Bailey, W. H. *et al. Synopsis of IEEE Std C95.1^{TM}-2019 IEEE Standard for Safety Levels With Respect to Human Exposure to Electric, Magnetic, and Electromagnetic Fields, 0 Hz to 300 GHz. IEEE Access* vol. 7 (2019).

Figures

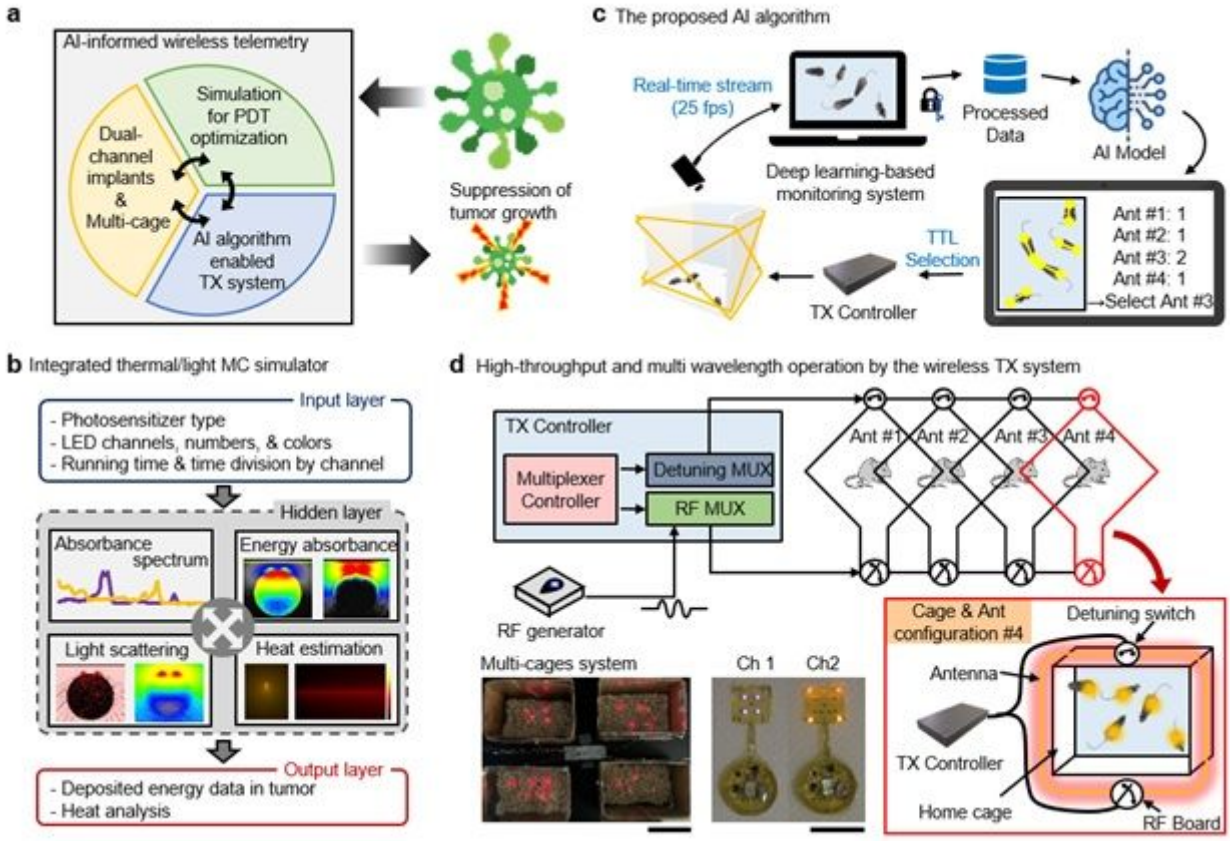

Figure 1

(a) Overview of the proposed integrated platform. (b) Workflow for an integrated MC simulator for analysis of heat dissipation and light propagation. (c) The proposed AI algorithm for real-time monitoring of mice. (d) Schematic illustration of the low-power wireless telemetry system for high-throughput and multi-wavelength operation (top). Two images represent demonstration of multichannel activation using a single power source (bottom to the left) and multi-wavelength operation (bottom to the right); scale bar 10 cm (left) and 1 cm (right).

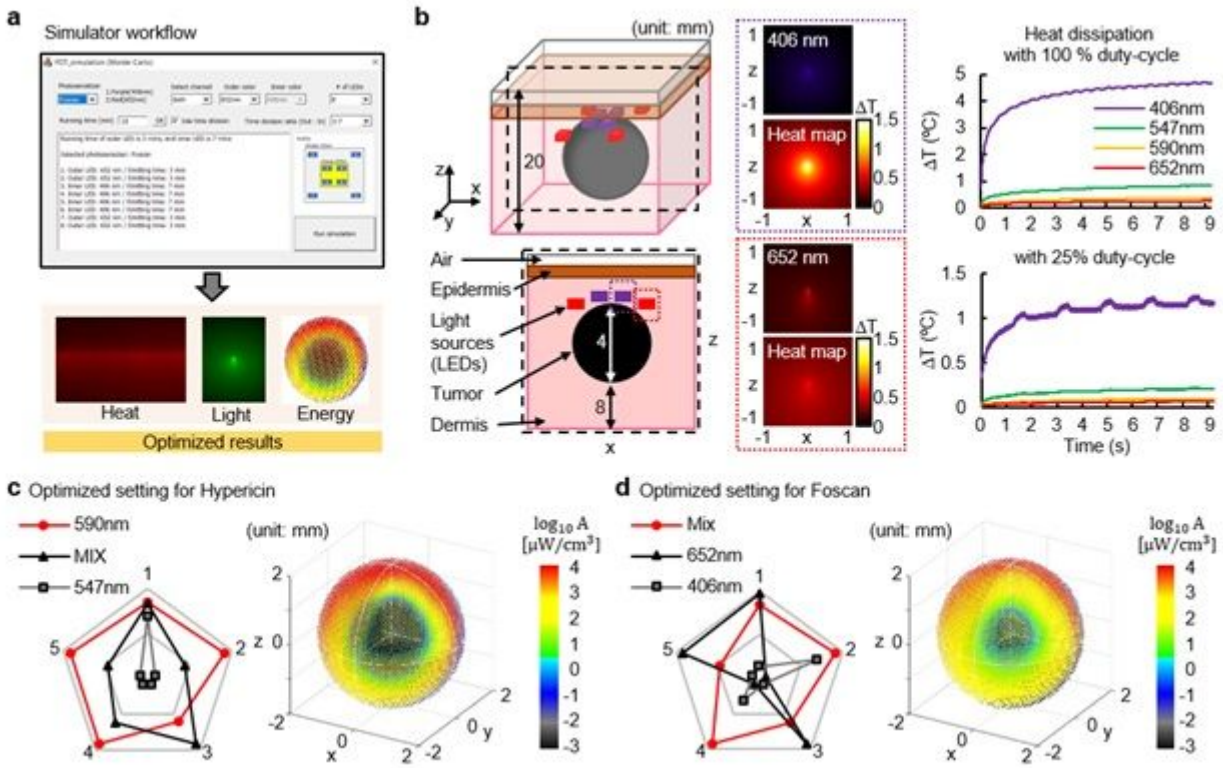

Figure 2

(a) Overview of the integrated MC simulator. The simulation platform processes parameters from a user and performs analysis of thermal dissipation, light propagation, and energy absorption. One can determine the best PDT regimen to be the most effective in activating a photosensitizer. (b) Three-dimensional and cross-sectional view of a tumor-tissue model (left). Light scattering and heatmap at a wavelength of 406 nm and 652 nm, respectively for activation of Foscan (middle). Plots of variation in temperatures as a function of time during each mode of operation; constant and 25 Hz with 10 ms on (right). The best PDT regimen for activation of Hypericin (c) and Foscan (d). Five criteria include 1. degree of light penetration, 2. rate of energy absorbance, 3. level of uniformity of energy absorbance into a tumor cell, 4. the time required for delivery of targeted light energy, and 5. range of temperature variation.

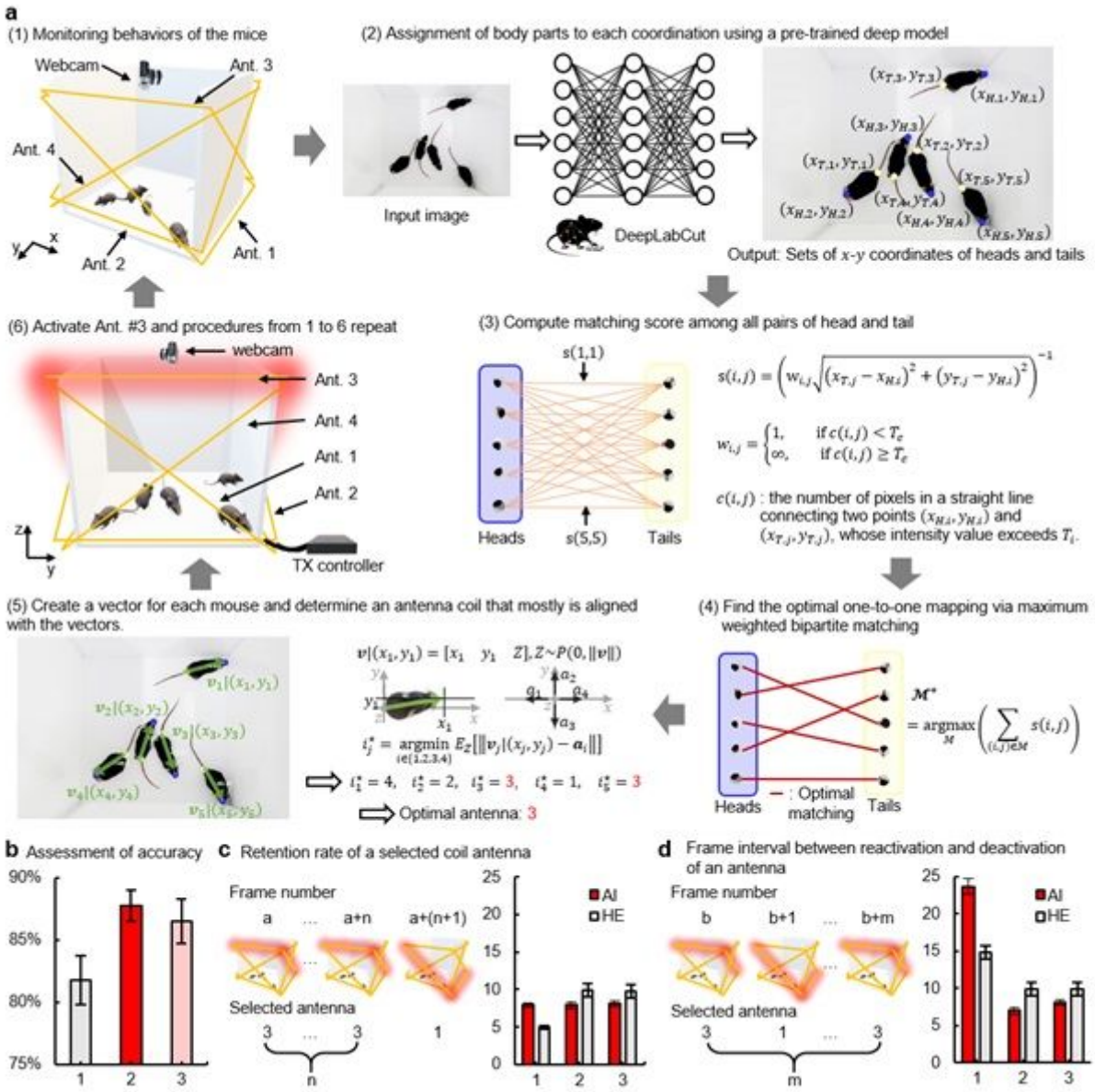

Figure 3

(a) Illustration of step-by-step procedures for the proposed artificial intelligence algorithm. (b) Assessment of detection accuracy for three different antenna structures: 1. 4-coil (each two coil antennas are on the x- and the y-axis, respectively), 2. Dual-coil (along the x-axis), and 3. Dual-coil (along the y-axis). Statistics of the number of frames for two representative cases; how long a selected antenna remains activated (c) and how many frames (how long an interval) exist between activation of an antenna and reactivation of itself after the first deactivation (d).

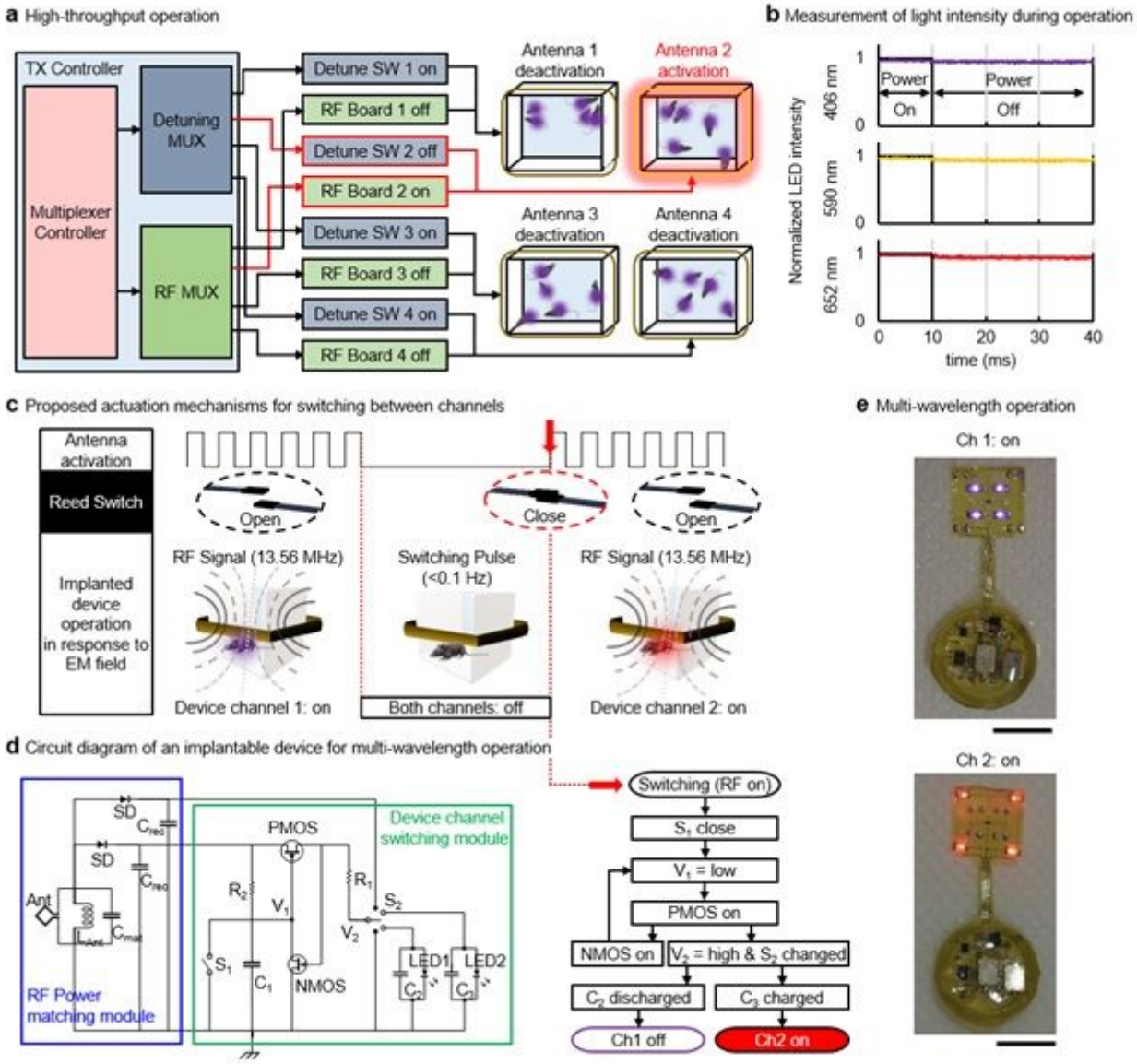

Figure 4

(a) Functional block diagram of high-throughput multi-cage control TX system. (b) Measurements of light intensity during the TX system operation. Devices maintain constant light intensity during operation. (c) Illustration of the proposed reed switched enabled actuation mechanism. (d) Circuit diagram of an implantable device for multi-wavelength operation. (e) Images of an implantable device with multi-wavelength operation; scale bar 5 mm.

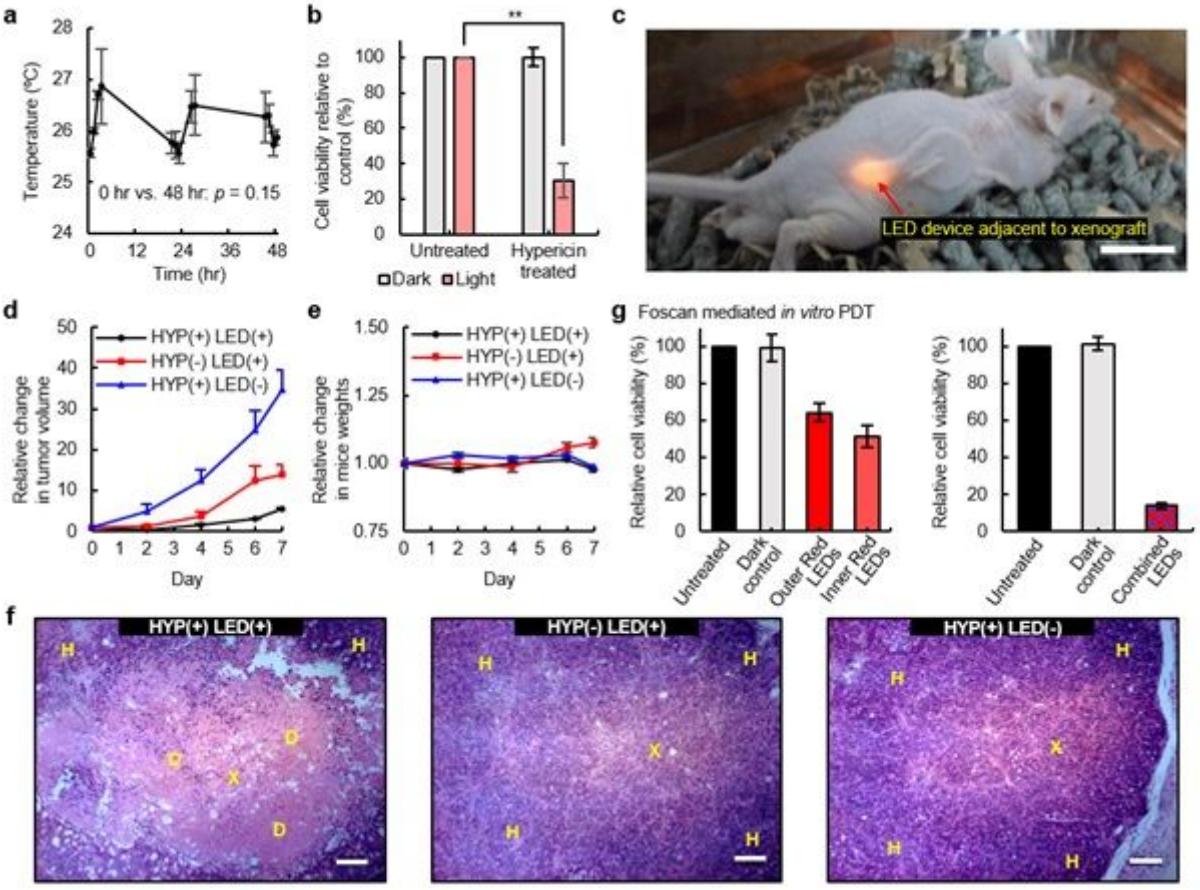

Figure 5

Hypericin mediated in vitro and in vivo PDT. (a) LED devices were continuously switched on and the operating temperatures of devices were measured over 48 hours. (b) HT29 cells were seeded into 24-well plates and incubated with 200 nM Hypericin in the dark. LED devices were positioned under the wells in the centre of the well and cells were treated with 36 mJ cm-2 of light (1 hour light treatment). After 24 hours, cell viability was assessed. Data are shown relative to control treated cells and represent means with SD of 3 independent experiments. **p<0.005. Subcutaneous HT29 tumor xenografts were generated in BALB/c nude mice. Mice were implanted with the LED devices adjacent to tumor xenografts. LED devices were switched on and Hypericin was administered every 24 hours for total doses of 3.5mg kg-1 of Hypericin and 12.1 J cm-2 of light. (c) Photograph of a mouse with a device implanted. Here, LEDs are positioned adjacent to tumor xenograft. (d) Tumor volumes and (e) weights of mice were recorded on Days 0, 2, 4, 6, and 7. HYP(-)LED(+) group received miniature LED light treatment only. HYP(+)LED(-) group received Hypericin treatment only. HYP(+)LED(+) group received both light and Hypericin treatments. (f) Tumor xenografts were harvested following in vivo PDT, fixed in 4 % PFA, embedded into paraffin, sectioned, and subjected to H&E staining; scale bar 100 µm. X = Xenograft, H = Healthy tissue and D = Dead tissue. (g) Foscan mediated in vitro PDT. HT29 cells were seeded into 24-well plates and incubated with 100 nM Foscan in the dark. Dual-channel LED devices were positioned under the wells and cells were treated with 1.8 mJ cm-2 of light. Dual-channel LED devices contained either all Red LEDs (1 hour continuous Red LED light treatment, left) or combined Red/Violet LEDs (30 mins outer red LEDs

treatment followed by 30 mins inner violet LEDs treatment, right). After 24 hours, cell viability was assessed. Data are shown relative to control treated cells and represent means with SD of 3 independent experiments.

Supplementary Files

This is a list of supplementary files associated with this preprint. Click to download.

- SupplementaryInformation.pdf
- Video1.mp4
- Video2.mp4